Provided for non-commercial research and education use.
Not for reproduction, distribution or commercial use.

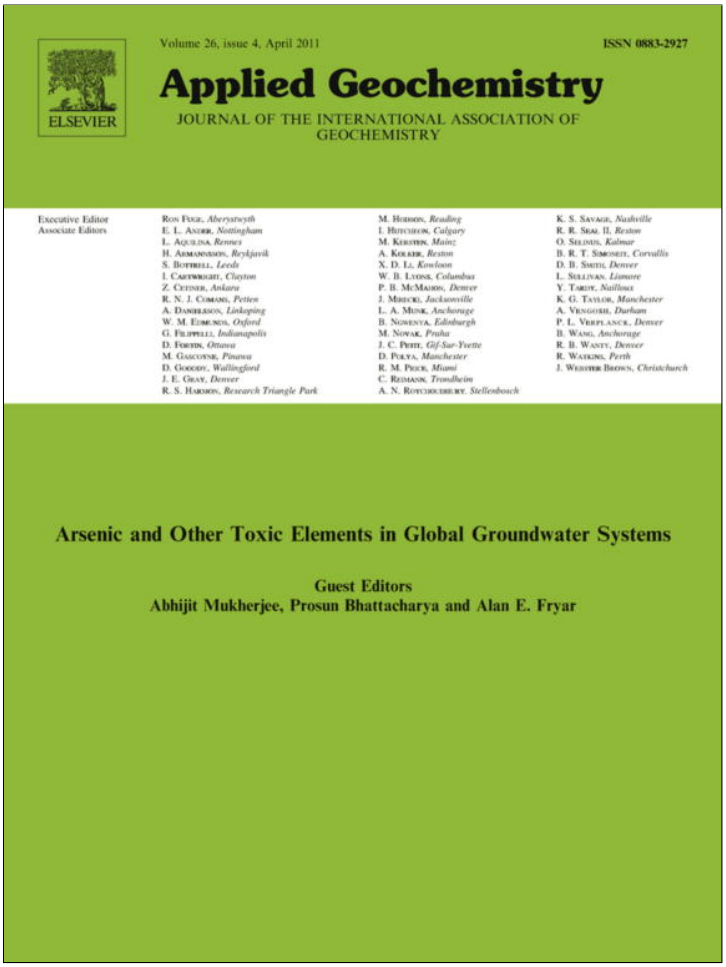

This article appeared in a journal published by Elsevier. The attached copy is furnished to the author for internal non-commercial research and education use, including for instruction at the authors institution and sharing with colleagues.

Other uses, including reproduction and distribution, or selling or licensing copies, or posting to personal, institutional or third party websites are prohibited.

In most cases authors are permitted to post their version of the article (e.g. in Word or Tex form) to their personal website or institutional repository. Authors requiring further information regarding Elsevier's archiving and manuscript policies are encouraged to visit:

http://www.elsevier.com/copyright

Applied Geochemistry 26 (2011) 484–495

Contents lists available at ScienceDirect

Applied Geochemistry

journal homepage: www.elsevier.com/locate/apgeochem

Particle-size dependence on metal(loid) distributions in mine wastes: Implications for water contamination and human exposure

C.S. Kim [a,*], K.M. Wilson [a], J.J. Rytuba [b]

[a] School of Earth and Environmental Sciences, Schmid College of Science, Chapman University, Orange, CA 92866, USA
[b] U.S. Geological Survey, Menlo Park, CA 94305, USA

ARTICLE INFO

Article history:
Available online 24 January 2011

ABSTRACT

The mining and processing of metal-bearing ores has resulted in contamination issues where waste materials from abandoned mines remain in piles of untreated and unconsolidated material, posing the potential for waterborne and airborne transport of toxic elements. This study presents a systematic method of particle size separation, mass distribution, and bulk chemical analysis for mine tailings and adjacent background soil samples from the Rand historic mining district, California, in order to assess particle size distribution and related trends in metal(loid) concentration as a function of particle size. Mine tailings produced through stamp milling and leaching processes were found to have both a narrower and finer particle size distribution than background samples, with significant fractions of particles available in a size range ($\leqslant$250 μm) that could be incidentally ingested. In both tailings and background samples, the majority of trace metal(loid)s display an inverse relationship between concentration and particle size, resulting in higher proportions of As, Cr, Cu, Pb and Zn in finer-sized fractions which are more susceptible to both water- and wind-borne transport as well as ingestion and/or inhalation. Established regulatory screening levels for such elements may, therefore, significantly underestimate potential exposure risk if relying solely on bulk sample concentrations to guide remediation decisions. Correlations in elemental concentration trends (such as between As and Fe) indicate relationships between elements that may be relevant to their chemical speciation.

© 2011 Elsevier Ltd. All rights reserved.

1. Introduction

Metals and metalloids often pose a threat to wildlife and human health in mine-impacted environments (EPA, 1997b; Wang and Mulligan, 2006). For example, the release of metal(loid)s from solid-phase mine wastes into surface and groundwaters may occur through multiple (and often related) processes including mineral dissolution, desorption of metal(loid)s from mineral surfaces, formation of stable aqueous metal(loid) complexes and secondary mineral (nano)precipitates, and colloidal transport. The subsequent exposure to metal(loid)s from water supplies affected by mining activity can lead to a number of adverse health effects that are both acute and chronic (Mandal and Suzuki, 2002; Plumlee and Ziegler, 2003). Additionally, the inadvertent ingestion or inhalation of metal(loid)-enriched soil, tailings, or dust can represent significant exposure pathways for humans and other organisms to potentially toxic elements in mine wastes. These mechanisms are of particular significance to children and infants, who are both more susceptible and sensitive to metal(loid) intake through such incidental exposures (Chou and De Rosa, 2003; Carrizales et al., 2006).

A number of factors influences the transport, distribution, speciation and bioavailability of toxic elements in the environment. One particularly important variable in assessing metal(loid) mobility from mine wastes is the size distribution of the material itself. Particle size (where a particle is defined here as a solid non-aggregated mineral(-like) grain) is a well-known determinant of transport potential by both aeolian (Carpi, 1997; Jackson, 1997) and fluvial (Lowry et al., 2004; Audry et al., 2006) processes, with smaller particles traveling farther from their source and becoming dispersed over a wider spatial range. It has also been shown that the trace metal(loid) content of mine wastes, soils and sediments can vary, sometimes dramatically, as a function of particle size, with an inverse relationship between particle size and concentration commonly observed (Harsh and Doner, 1981; Moore et al., 1989; Mullins and Norman, 1994; Kim et al., 2004; Westerlund and Viklander, 2006; Moreno et al., 2007). Furthermore, particle size effects may influence the reactivity of metal(loid)s in mine wastes, with finer-grained particles possessing higher available surface areas and, therefore, enhanced solubility in aqueous media, including lung and gastric fluids.

No known studies have systematically addressed the effects of particle size on the concentration, speciation and reactivity of toxic metal(loid)s in mine wastes, despite the fact that size distribution

* Corresponding author.
E-mail address: cskim@chapman.edu (C.S. Kim).

0883-2927/$ - see front matter © 2011 Elsevier Ltd. All rights reserved.
doi:10.1016/j.apgeochem.2011.01.007

is one of the primary variables controlling the transport and dispersion of waste materials from mine sites. Such information may, therefore, serve as a diagnostic tool for predicting the potential mobility of metal(loid)s from mine wastes and determining enrichment and loss patterns of elements through weathering or other processing mechanisms. Environmental assessments of mine-impacted ecosystems can benefit from such an approach because of the commonly elevated metal(loid) concentrations present and the corresponding environmental concerns typically associated with mining regions.

Currently, cleanup decisions and activities at mine sites are based primarily on the comparison of bulk sample concentrations against established regulatory screening levels (EPA, 1997a) under the assumption that such levels are sufficiently protective of biota and humans. However, it is additionally important to characterize the relationship between particle size and concentration within a contaminated sample because regulatory levels can be exceeded in specific size fractions, including those that are most readily ingested or inhaled. The development of effective remediation strategies at mine sites should, therefore, consider particle size/concentration relationships and correlations in particle size-dependent element concentration trends that may affect their chemical speciation, reactivity and potential bioavailability.

The objective of this study is to present a systematic method of particle size separation, mass distribution, and chemical analysis for heterogeneous geological materials, thereby providing size-dependent characterization of a sample with considerably more detail than is available through bulk concentration measurements. Such a characterization establishes a basis for understanding trends between trace metal(loid) concentrations and particle size, and identifying statistically significant correlations between metal(loid)s exhibiting similar concentration trends. This analysis is applied to mine waste and associated background samples from the Randsburg historic mining district in California as a case study to assess the extent of metal(loid) contamination in this region.

2. Materials and methods

2.1. Site description

Mine waste samples were collected in the Randsburg historic mining district located in the Mojave Desert of south-central California (Fig. 1), specifically in and around the adjoining towns of Randsburg, Johannesburg and Red Mountain. The Rand Mountains are composed primarily of schists that have been intruded by younger plutonic rocks of quartz monzonite and by a later series of shallow dikes of diabase and rhyolite–latite (Hulin, 1925). The poorly consolidated Rosamond series are sedimentary continental rocks consisting of stratified conglomerates, feldspathic sandstones and clays that outcrop and underlie economic mineral deposits (Au, Ag, W) near the town of Red Mountain. Lakebed sediments, in part derived from the Rosamond series sediments, underlie the area covered by the Red Mountain volcanics. The mining district experiences sparse and intermittent rainfall averaging 17.4 cm/a.

In addition to Au and Ag ore mined and processed in this region during the late 19th/early 20th century, elevated levels of other metal(loid)s, specifically As, were identified to have been concentrated simultaneously with these precious metals as dissolved species in hydrothermal solutions prior to deposition in quartz veins (Rytuba et al., 2007). Excavated ore from the Randsburg mining district was initially passed through stamp mills which pulverized the ore to a fine grain size in the presence of elemental liquid Hg to amalgamate the Au and Ag, which was typically present as native Au, native Ag, and electrum, a Au/Ag alloy. Subsequent processing efforts used a cyanide leach to reprocess the stamp mill tailings and recover the remaining Au and Ag.

2.2. Sample collection and processing

Sample media collected in the Randsburg historic mining district included processed mine tailings, unprocessed waste rock, and "background" soil samples located a significant distance (1.4–2.6 km) from the tailings piles. Approximately 2–3 kg of material were collected at each sampling site, with the top several cm of sample removed prior to sample collection to avoid sampling the most highly weathered material and to access material most representative of the entire pile. Similarly, the top 5 cm of material was removed at background sample sites in order to avoid sampling the most directly exposed material that may have been most recently contaminated by adjacent tailings piles through windborne and/or fluvial particle transport. Samples were collected in plastic bags and following the size separation described in the following paragraph, individual size fractions were stored in borosilicate glass jars with Teflon lids. Each sample was mixed periodically as it was air-dried in a fume hood for a minimum of 24 h and its total mass weighed prior to size separation. Oven drying was not conducted in order to minimize potential mineralogical transformations as a result of heating at elevated temperatures. For the purposes of this study, analysis will be presented for samples taken from tailings piles at the Solomon Mine (SM-MT) and the Descarga (D-MT) mine tailings dam as well as background soil samples (SM-BG, D-BG) collected some distance away but in the direction of prevailing winds from the respective tailings piles (Fig. 1).

Samples were passed through a series of 10 stainless steel 13″ sieves featuring increasingly finer meshes using a Ro-Tap Model B testing sieve shaker from Tyler Industrial Products which agitated each sample for a minimum of 30 min to ensure effective size separation, resulting in 11 distinct size fractions (Table 1). The sieve stack was tightly taped along the interfaces between the sieves and double-bagged in construction-grade garbage bags to minimize the potential loss and dispersal of the finest-grained particles during the agitation process. The stack was then disassembled and each size fraction recovered and weighed individually. The sum of the individual fractions typically varied by $\leqslant$0.7% from the initial weighed mass, confirming that very little of the sample was lost during sieving. Scanning electron microscopy (SEM) and energy dispersive X-ray spectroscopy (EDS) was conducted using LEO 982 Digital Field and Philips XL-30 FEG scanning electron microscopes (both equipped with EDAX EDS systems) on selected size fractions. The resulting SEM images were used to verify the size distribution of the size fractions generated while energy-dispersive X-ray spectra provided information regarding the chemical composition of individual particles.

To determine the bulk mineralogy in tailings and background samples, X-ray diffraction was conducted on selected size fractions using Beamline 11-3 of the Stanford Synchrotron Radiation Lightsource (SSRL). Samples were dispersed on a piece of clear Scotch tape and sealed with a second piece of tape. Diffraction images were collected for a period of 2 min at an energy of 12,705 eV (wavelength 0.9758 Å) with a 1° rocking angle during data collection. Calibration was conducted with a LaB_6 powder standard. Integration of diffraction images was performed using the freeware program FIT2D (Hammersley, 2004) and peak fitting/phase identification of resulting diffraction patterns using Jade version 6.

Splits of 5–10 g from the initial bulk sample and from each fraction size weighing >5 g were sent to ALS Chemex, a private analytical laboratory, where the bulk sample and splits S1–S7 were pulverized using a ring mill prior to digestion and analysis such that >85% of the sample passed through a 75 μm (Tyler 200 mesh)

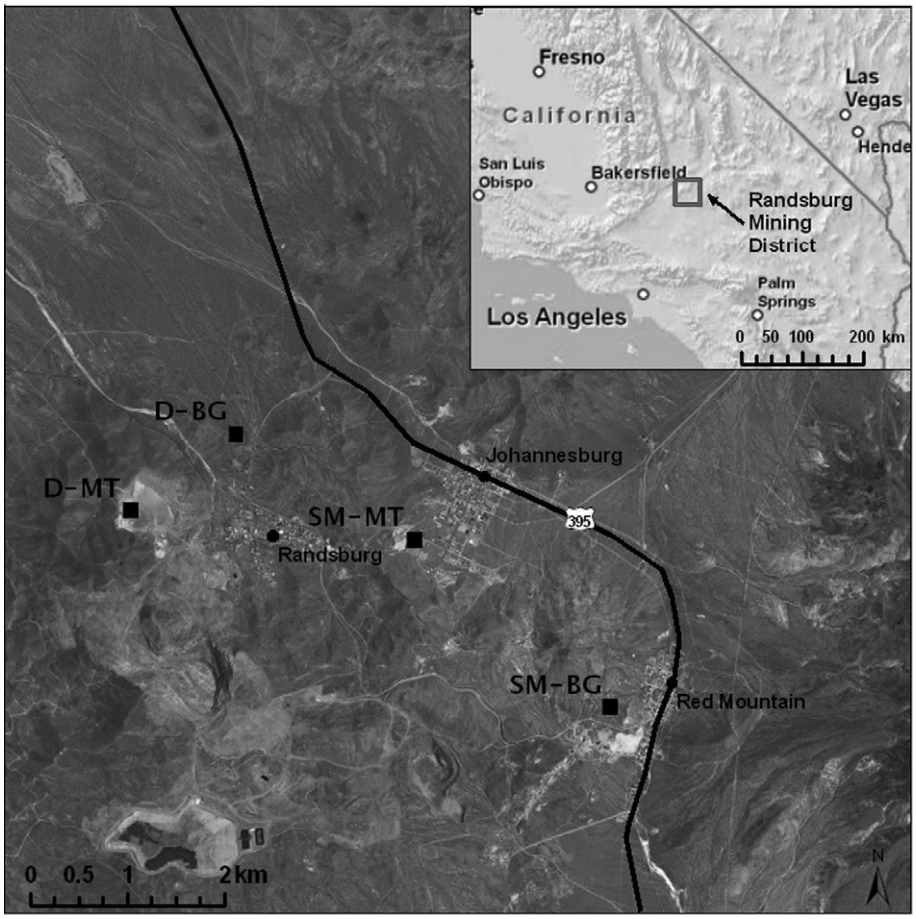

Fig. 1. Map indicating the location of the Randsburg historic mining district in the western Mojave Desert (inset) and sampling locations.

Table 1
Particle size diameter (d_p) ranges for each fraction size generated through dry sieving.

Size fraction	Particle diameter (d_p)
S1	$d_p > 2830$ μm
S2	2830 μm > $d_p > 1700$ μm
S3	1700 μm > $d_p > 1000$ μm
S4	1000 μm > $d_p > 500$ μm
S5	500 μm > $d_p > 250$ μm
S6	250 μm > $d_p > 125$ μm
S7	125 μm > $d_p > 75$ μm
S8	75 μm > $d_p > 45$ μm
S9	45 μm > $d_p > 32$ μm
S10	32 μm > $d_p > 20$ μm
S11	$d_p < 20$ μm

screen, ensuring that all size fractions could be comparably digested. A prepared sample (0.250 g) from each size fraction was then digested with $HClO_4$, HNO_3 and HF at 185 °C to near dryness and then further digested in a small volume of HCl. The solution was brought up to a final volume of 12.5 mL with 11% HCl, homogenized, and analyzed by inductively coupled plasma-mass spectrometry (ICP-MS) using a Perkin Elmer Elan 9000 spectrometer and/or inductively coupled plasma-atomic emission spectroscopy (ICP-AES) using a Varian Vista-PRO/Vista-725ES for a suite of 49 elements. The instrument detection limits and relative standard deviations for the elemental results presented in this manuscript are as follows: As (0.2 ppm/12.0%), Cr (1 ppm/13.6%), Cu (0.2 ppm/10.3%), Fe (0.01%/10.3%), Pb (0.5 ppm/11.7%) and Zn (2 ppm/12.1%). A series of two standards, one duplicate, and one blank were run within every 40 samples with standard and duplicate tolerances of 10% for quality control purposes.

2.3. Data analysis

The resulting concentration and mass data from the size separation step were systematically processed for each sample as follows:

(i) *Mass distribution*: A graph of sample mass distribution was generated plotting % mass of the sample against particle size fraction.
(ii) *Concentration distribution*: A series of graphs was generated plotting the concentrations of individual elements against particle size fraction.
(iii) *Concentration trend categorization*: Based on the concentration graphs generated, trends observed in concentration as a function of particle size were assigned for each element. This allowed each element's placement into one of the eight designated classification categories shown in Fig. 2, resulting in elemental groupings expressing similar concentration trends. These empirically-determined categories are consistent with patterns observed and described either by known parametric statistical distributions or by combinations of specific distributions (Evans et al., 2000). Such groupings suggest that elements with the same distribution trends may be directly associated with one another as a result of one or more possible factors which are addressed in the following section.

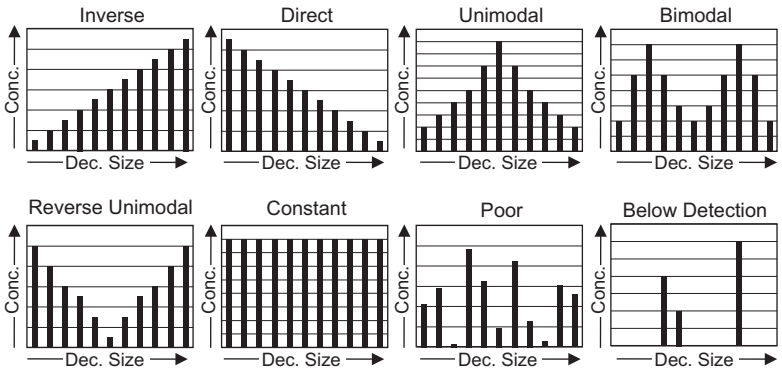

Fig. 2. Schematic of potential trends between particle size (*x*-axis, with size decreasing from *L*–*R*) and elemental concentration (*y*-axis).

(iv) *Elemental mass distribution*: A similar series of graphs to the concentration graphs was generated by plotting elemental mass distribution against particle size fraction, with elemental mass distribution determined using the following formula:

$$M\%_{e,i} = \frac{C_{e,i} * M\%_i}{\sum_{i=1}^{11} C_{e,i} * M\%_i} \quad (1)$$

where $M\%_{e,i}$ is the percent by mass of element *e* in size fraction *i*, $C_{e,i}$ the concentration of element *e* in size fraction *i*, and $M\%_i$ is the percent mass of the sample in size fraction *i*.

(v) *Statistical correlation*: The statistical analysis software JMP (2007) was used to generate an elemental correlation matrix from the concentration data, with each cell expressing the linear correlation coefficient (*r* value) for any two elements. The data within each cell was also encased in a 95% bivariate normal density ellipse where stronger correlations are represented visually by a collapsing of the ellipse along the diagonal axis (JMP, 2007). Cell values were then sorted to determine the strongest correlation among all elements as well as subsets of selected elements ranking the relative strength of association between one element and all other elements in the dataset.

3. Results and discussion

3.1. Size-based mass distribution analysis

Mass distribution plots for samples of both mine tailings and background material from the Solomon and Descarga sites are shown in Fig. 3, with the corresponding mass distribution data included in Table 2. These plots represent the particle size distributions based on sample mass, which vary depending on both sample type and location. For example, the tailings samples display much narrower size distributions, with splits S4–S6 (125–1000 μm) representing 82.0% and 76.9% at the Solomon and Descarga tailings by mass, respectively. In contrast, splits S4–S6 of the corresponding background samples only constitute 48.4% and 45.3% of their respective sample mass. The background samples generally display relatively broad particle size distributions, with the majority of the size fractions representing $\geqslant\sim$10% of the entire sample mass, while only three of the 11 size fractions reach this level in the tailings samples (specifically, splits S4–S6).

This difference in size distribution between the two types of samples reflects the stamp milling process to which the tailings were initially subjected, which utilized heavy steel plates to crush the Au and Ag ore into finer-grained material more appropriate for extraction by either Hg amalgamation or cyanide heap leaching. Stamp milling was successful in converting newly-excavated ore material of variable size into a more uniformly fine sand-sized material of average particle size $\sim$250 μm.

The mass distribution analysis also provides insight into the proportions of finer-grained material that may be bioaccessible in a given sample through ingestion or inhalation pathways. Solid particles $\leqslant$250 μm (corresponding to size fractions S6–S11) can readily adhere to surfaces including those of skin and food (Plumlee and Ziegler, 2003) and be subsequently ingested during food consumption, while particles <10 μm (represented in part by S11, which is actually comprised of particles <20 μm) can be passively inhaled, with the smallest particles ($\leqslant$2.5 μm) deeply penetrating the alveoli in lungs (Plumlee and Ziegler, 2003; Plumlee et al., 2006). While none of the <20 μm fractions of the four samples shown represents more than 1% of the samples by mass, the <250 μm fractions collectively comprise between 25.3% and 61.4% of the mass of samples (Table 2). This suggests that the incidental ingestion of particles that have adhered to skin, clothing, or food may be a significant pathway of metal(loid) exposure for both types of samples.

3.2. X-ray diffraction

Results from XRD analysis of selected sample size fractions are provided in Table 3. Quartz (α-SiO_2) is identified in all size fractions investigated, with calcite ($CaCO_3$) and lepidocrocite (γ-FeOOH) identified sparingly. These commonly-occurring minerals are consistent with the presence of weathered schists and the sedimentary rocks of the Rosamond series. In particular, the abundance of quartz reflects the original rock types present as well as the later quartz monzonite intrusions and quartz vein deposits that formed in this region. No clear trend in mineralogical composition as a function of particle size could be detected, and no discernible mineralogical differences are apparent between the tailings and the background samples, most likely due to (1) the proximity of the sample types to one another and (2) the relatively minor differences in precious metal concentrations required to categorize material as ore compared to waste rock or background samples. Notably, none of the primary matrix minerals identified by XRD contains in their stoichiometries any of the metals or metalloids investigated and analyzed in the following section (excepting Fe, which is naturally abundant), confirming that these elements are present in trace quantities and/or in phases that cannot be readily identified using bulk X-ray diffraction methods.

3.3. Scanning electron microscopy

Scanning electron microscopy analysis of selected size fractions from the D-MT sample (Fig. 4) verifies that the size fractions are

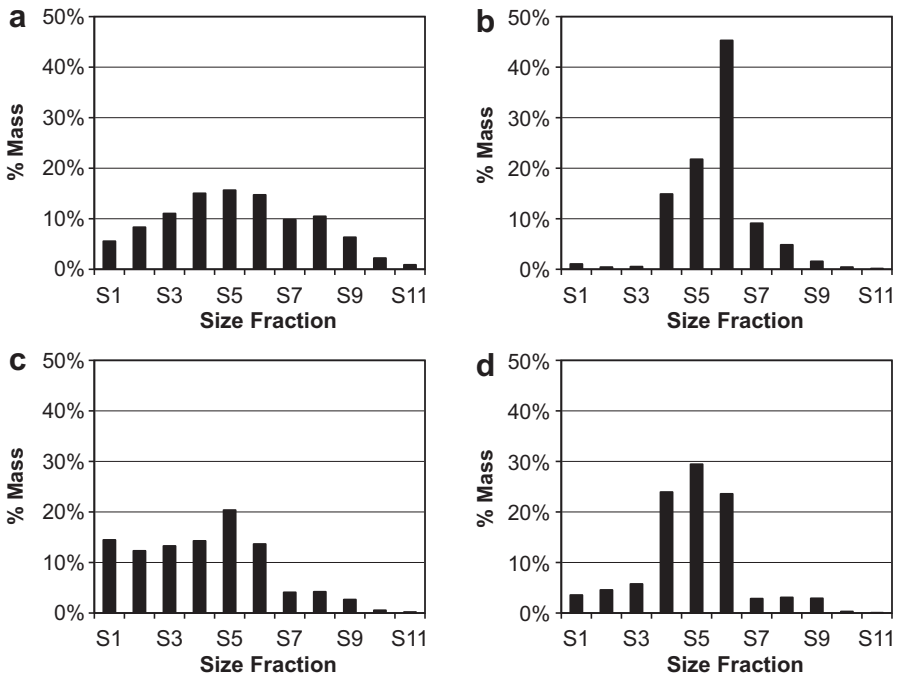

Fig. 3. Total sample mass distribution by particle size fraction for the (a) Solomon Mine background (SM-BG), (b) Solomon Mine tailings (SM-MT), (c) Descarga background (D-BG), and (d) Descarga tailings (D-MT) samples. Refer to Table 1 for a description of the particle size ranges corresponding to each labeled size fraction S1–S11.

Table 2
Mass distribution of samples as a function of particle size resulting from size separation by dry sieving.

	SM-BG (%)	SM-MT (%)	D-BG (%)	D-MT (%)
S1	14.5	1.0	5.5	3.6
S2	12.3	0.4	8.3	4.6
S3	13.3	0.5	11.0	5.7
S4	14.3	14.9	15.0	23.9
S5	20.4	21.8	15.6	29.4
S6	13.7	45.3	14.7	23.6
S7	4.1	9.1	9.8	2.8
S8	4.2	4.8	10.5	3.1
S9	2.7	1.6	6.3	2.9
S10	0.5	0.4	2.2	0.3
S11	0.2	0.1	0.9	0.1

comprised primarily of particles in the expected size range and not of substantial fractions of multi-particle aggregates nor particles outside of this size range. Among the coarser size fractions, however, considerable numbers of fine-grained particles, typically smaller than the dedicated size range, can be observed attached to coarse particle surfaces. Both back-scattered electron (BSE) imaging and EDS analysis indicates that the smaller particles are consistent with the larger particles to which they are attached, and are thus not thought to represent significant contributions to the elemental concentration trends discussed in the following sections.

BSE imaging reveals discrete particles which appear lighter in color, indicating higher degrees of backscattering and enrichment in higher-Z elements relative to the majority of particles. These "brighter" particles are typically within the expected size range of that particular size fraction and appear to increase in abundance with decreasing particle size (Fig. 4a–c). EDS analysis of selected high-backscattering particles reveals that the higher-Z elements include Ca, Fe and As in addition to the presence of O, Al, and Si, which are common among all particles (see EDS spectra in Fig. 4). The enrichments in Ca, Fe, and As are consistent with the XRD-based identification of calcite, lepidocrocite, and other Ca-bearing phases (Table 3) but also may indicate the presence of

Table 3
X-ray diffraction peak matching results of selected size fractions from all samples.

Sample	Mineral(s) identified	Mineral formula
SM-BG		
S5	Quartz	SiO_2
S7	Calcite	$CaCO_3$
S9	Quartz	SiO_2
	Berlinite	$AlPO_4$
	Calcite	$CaCO_3$
	Lepidocrocite	β-FeOOH
S11	Quartz	SiO_2
	Howlite	$Ca_2SiB_5O_9(OH)_5$
	Hexahydroborite	$Ca(B(OH)_4)_2(H_2O)_2$
	Brushite	$CaHPO_4(H_2O)_2$
SM-MT		
S5	Quartz	SiO_2
	Calcite	$CaCO_3$
S7	Quartz	SiO_2
	Calcite	$CaCO_3$
S9	Quartz	SiO_2
S11	Quartz	SiO_2
	Howlite	$Ca_2SiB_5O_9(OH)_5$
D-BG		
S7	Quartz	SiO_2
	Berlinite	$AlPO_4$
	Lepidocrocite	β-FeOOH
S9	Quartz	SiO_2
	Berlinite	$AlPO_4$
S11	Quartz	SiO_2
D-MT		
S5	Quartz	SiO_2
S7	Quartz	SiO_2
S9	Quartz	SiO_2
	Carnotite (anhyrd.)	$K_2(UO_2)_2V_2O_8$
S11	Quartz	SiO_2

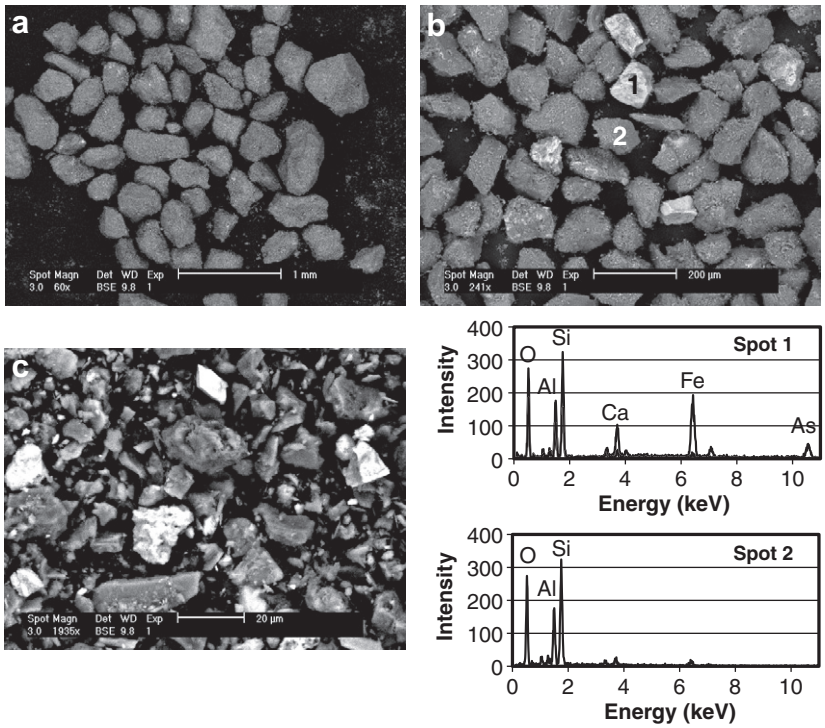

Fig. 4. Backscattered electron (BSE) micrograph images of the (a) S5 (250–500 μm), (b) S7 (75–125 μm) and (c) S11 (<20 μm) size fractions of the Descarga mine tailings (D-MT) sample. Energy dispersive spectra of selected particles in the S7 size fraction are shown at bottom right.

phases such as arseniosiderite ($Ca_2Fe_3(AsO_4)_3O_2{\cdot}3H_2O$) or yukonite ($Ca_3Fe(AsO_4)_2(OH)_3{\cdot}5(H_2O)$). The abundance of O, Al, and Si along with the occasional detection of Na, Mg and K indicates the presence of aluminosilicate phases such as clays and feldspars. However, such phases were not identified by XRD analysis, suggesting either that the aluminosilicate phases may be poorly crystalline and/or amorphous, as documented in previous studies (Eggleton, 1987; Penn et al., 2001), or that synchrotron-based XRD analysis is not an optimal strategy for detecting such phases.

3.4. Size-based concentration analysis

As each sample analyzed yields nearly 50 separate plots of elemental concentration as a function of particle size, only selected elements are discussed in this study: As, due to its high level of enrichment and related health concerns, and other trace metals commonly associated with the mineralization of precious metals found in this region. Fig. 5 shows size-dependent concentration plots for As, Cr, Cu, Fe, Pb and Zn for the four different sample locations. The average bulk concentrations of these respective elements in each sample are indicated as horizontal dotted lines on each plot. Complete analytical data for the elements investigated in this study are available as online Supplementary material.

Significant trends in elemental concentration are displayed in these individual plots that are distinctive from the mass distribution trends of samples. For instance, for most of the selected elements the highest concentrations are found in the smallest particle size range, which usually represents the smallest percentage mass of the sample. This suggests that two sets of processes are at work: those that separate a sample into a range of particle sizes which can be characterized by mass, and those that differentiate a sample by chemical composition within and across those different particle size fractions. Both physical and chemical reactions are likely to play a role, perhaps to different degrees, in order to generate the separate mass and concentration distribution trends observed. With reference to Fig. 2, the following discussion provides possible explanations for each of the concentration trends observed among multiple samples and elements.

(i) *Inverse*: An inverse relationship between particle size and elemental concentration shows that the element becomes preferentially concentrated in progressively finer size fractions. This trend is consistent with the element occurring in one or more phases that are highly insoluble and persist during the chemical weathering and breakdown of material relative to the other matrix phases present. If the dominant element-bearing phase(s) (EBP) additionally exhibits a low mineralogical hardness, physical weathering processes will further concentrate the EBP into progressively finer grain size fractions. Alternatively, an inverse trend would result from the element existing as a sorbed species, e.g. As(V) sorbed to Fe oxyhydroxides, where the proportion and/or surface area of the sorbent phase increases with decreasing particle size.

(ii) *Direct*: A direct relationship between particle size and elemental concentration is formed when the element becomes more depleted in progressively smaller size fractions. This trend is consistent with a highly soluble and/or mineralogically hard EBP, which would be dissolved rapidly and removed during the weathering process and/or physically weathered at a slower rate than other matrix minerals. Increased surface areas among smaller particles and encapsulation of soluble EBPs within larger particles would also contribute to differential weathering rates across the various size fractions.

(iii) *Unimodal*: A concentration trend that reaches a maximum in an intermediate grain size fraction, and features declining concentrations with both increasing and decreasing grain size from that size fraction, may indicate the presence of an EBP that is in the process of becoming concentrated in progressively finer size fractions en route to an eventual inverse relationship. Such a trend might also develop if the

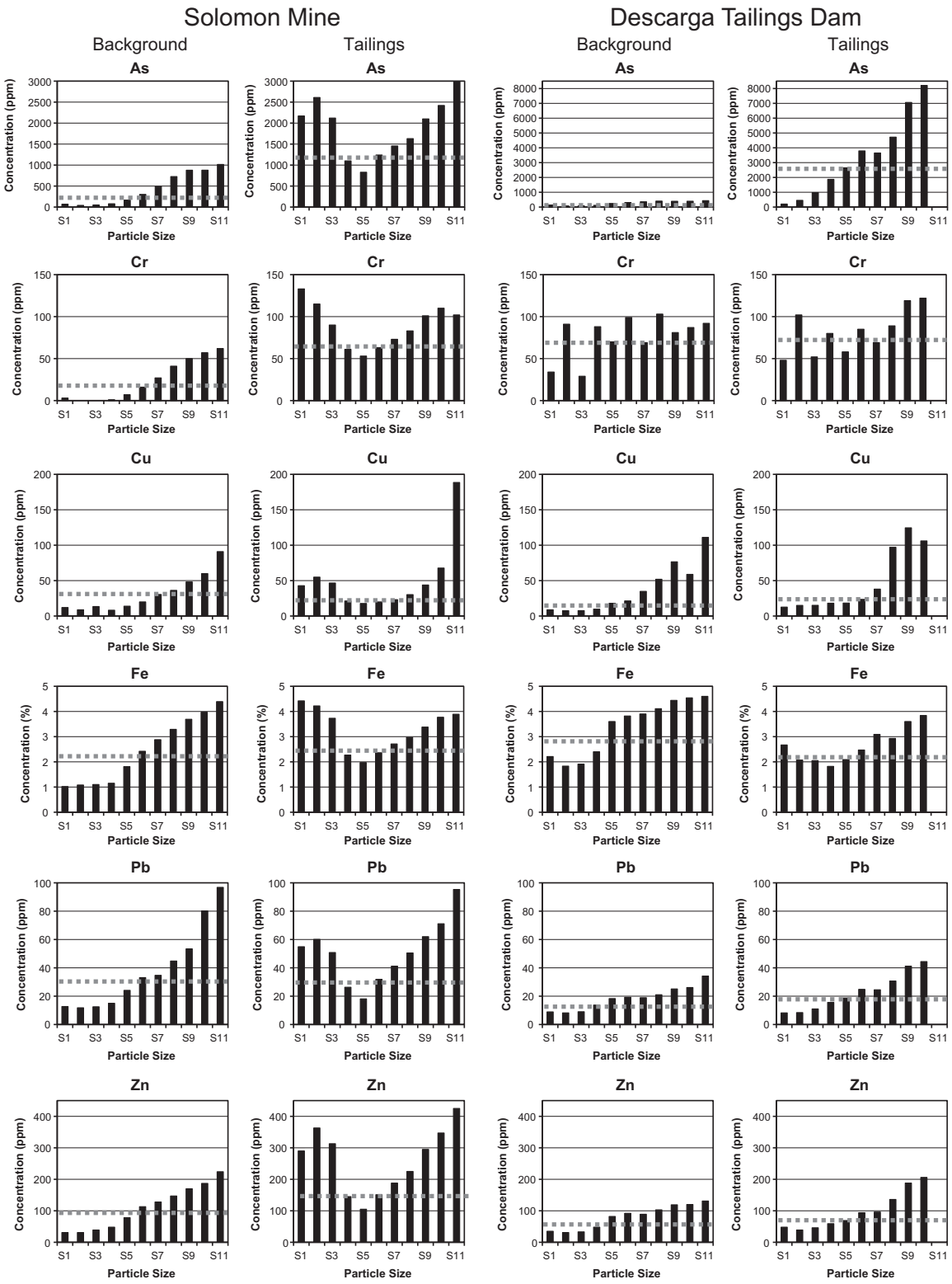

Fig. 5. Concentrations of selected elements in the Solomon and Descarga background and mine tailings samples as a function of particle size. The average bulk concentration of each element in each sample is designated on the plots by a horizontal dotted gray line. Refer to Table 1 for a description of the particle size ranges corresponding to each labeled size fraction S1–S11.

average initial crystal/particle size of formation for the dominant EBP in the system coincided with the size range represented by the intermediate size fraction.

(iv) *Bimodal*: A trend that reaches relative maxima in two separate, non-adjacent intermediate grain size fractions would most likely be observed in a sample with at least two

distinct EBPs, each with either its own (different) crystal size of formation or rate of weathering that allows them to progress towards inverse relationships at different rates.

(v) *Reverse Unimodal*: This trend, in which the concentration of a selected element reaches a minimum in an intermediate grain size fraction, may be indicative of the presence of two separate EBPs with opposing concentration trends; i.e., one phase may display an inverse relationship, whereas the other may display a direct relationship between particle size and element concentration. The resulting combination of the two trends would cause the reverse unimodal trend observed. It may be difficult to distinguish between bimodal and reverse unimodal elemental distributions due to their relative similarity in appearance.

(vi) *Constant*: A constant elemental concentration with varying particle size indicates that there is no size dependency on concentration and that the element is unperturbed by physical and chemical weathering processes that would otherwise preferentially concentrate the element into specific size fractions. The EBP may constitute a large proportion of the sample matrix or have similar solubility and hardness characteristics of the matrix, and thus is likely to be equally abundant in all size fractions.

(vii) *Poor*: No discernible trend or relationship can be observed in elemental concentration as a function of particle size. This often occurs when concentrations are extremely low and close to the detection limit of the instrument, and/or the quantities of particles in certain size fractions are small.

(viii) *Below Detection*: More than half of the size fractions feature concentrations of the element that are too low to detect by ICP-MS or ICP-AES, thus impairing the ability to identify meaningful trends as a function of particle size.

A qualitative review of the concentration plots and subsequent association of each element into one of the above designated categories results in groupings of elements that share similar size-dependent trends (e.g. the D-MT sample in Table 4). These groupings suggest possible correlations between elements; conversely, they can also indicate the absence of correlations between elements that feature different concentration trends. Reasons for two elements sharing similar concentration trends may include, but are not limited to: (a) co-existing in mineral form (e.g. $FeAsO_4$, where Fe and As are correlated); (b) the presence of sorbed species (e.g. Cu sorbed to Fe oxide phases, Kooner, 1992; Peacock and Sherman, 2004); (c) the formation of (co-) precipitates (e.g. Zn–Al layered double hydroxides, Towle et al., 1997; Roberts et al., 2003; Nachtegaal and Sparks, 2004); and (d) inclusion as substituted ions into other mineral structures such as clays, sulfides and metal (hydr)oxides (Manceau et al., 2000; Savage et al., 2000; Scheinost et al., 2002; Blanchard et al., 2007).

More detailed comparisons of concentration trend behaviors between the selected elements among the two mine sites (Fig. 5) reveal that elements across three of the four samples (SM-BG, D-BG, D-MT) display inverse concentration trends with particle size, suggesting that they persist as relatively insoluble or soft phases into the finer-grained fractions and/or are present as sorbed phases, e.g. to Fe-(hydr)oxides. In contrast, the elements in the SM-MT sample display either reverse unimodal or bimodal concentration trends. This is likely a result of, as described earlier, two or more EBPs in the sample with variable solubilities and/or hardness such that one phase is most concentrated in the finest size fraction (S11) and the other is concentrated in the coarse size fraction (S1 or S2).

Both the average concentrations as well as the concentration ranges of As are dramatically greater in both tailings samples compared to their respective background samples because of the concurrent deposition of this metalloid during the formation of the Au and Ag ores mined in this region (Rytuba et al., 2007). The enrichment of As in the finest size fractions of the tailings is of particular environmental concern as both wind and runoff water can serve to mobilize fine-grained tailings. In addition, ingestion and inhalation of airborne tailings particles represent potential As exposure pathways. The other trace metals (Cr, Cu, Pb, Zn) show more comparable concentration averages and ranges when comparing tailings with background samples, indicating that they exhibit considerably less enrichment in the ore deposits than As.

Fig. 5 also demonstrates that in all samples, the elemental concentrations of certain size fractions (particularly the finer size fractions of samples demonstrating an inverse trend) regularly exceed the average bulk concentrations of those elements in the sample as a whole. To summarize this quantitatively, Table 5 shows the average enrichment of the S6–S11 size fractions (corresponding to the readily ingestible $\leqslant$250 μm particle size range) over the bulk averages for those elements. Likewise, Table 6 shows the enrichment of elements in the finest size fraction (corresponding to the readily inhalable particle size range, and typically the most concentrated size fraction in a sample) relative to the bulk average concentrations.

These data show that the potentially ingestible and inhalable particles within a given sample are consistently enriched in the trace metal(loid)s above the level that would otherwise be predicted based on bulk chemical analysis of a bulk grab sample. On average, the $\leqslant$250 μm particles in the background and tailings samples were enriched by 86% and 79%, respectively, over their respective bulk elemental concentrations. Similarly, the finest size fractions in the background and tailings samples surpass their respective average bulk concentrations by 169% and 190%, respectively. There is no consistent difference between the extent of enrichment between tailings and background samples from the two locations; however, from both Tables 5 and 6 it is clear that across all samples, Cu is most significantly enriched in the fine-grained size fractions followed by As, suggesting that both elements are present in phases that are readily concentrated in the finer size fractions, while Fe shows the lowest extent of enrichment consistent with its presence as a primary (non-trace) element of considerable abundance in all size fractions. In the absence of such a size-dependent analysis, only bulk concentrations of contaminated samples would be compared to regulatory screening levels, likely underestimating the actual trace element concentrations of the more labile size fractions and resulting in incorrect assessments as to whether remedial actions should be taken at a particular tailings site.

3.5. Size-based elemental distribution analysis

Elemental mass distributions (calculated as shown in Eq. (1)) demonstrate the relative influences of sample mass distribution and elemental concentrations on the size fraction(s) in which a specific element is most abundant; this is distinct from the prior mass distribution analysis, which represents the size distribution of the material without any chemical information included. Plots displaying the % mass distributions of As, Cr, Cu, Fe, Pb and Zn as a function of particle size are shown in Fig. 6. These elemental mass distribution plots are clearly more influenced by and resemble more closely their corresponding sample mass distribution profiles (Fig. 3) than their respective elemental concentration trends (Fig. 5). This is due to the much larger degree of variation in the mass distribution, where the mass percentages regularly vary by over two orders of magnitude between the smallest and largest mass fractions, compared to that of the elemental concentrations, which typically only vary by a factor between 2 and 10.

Table 4
Categorization of elemental concentration trends for the Descarga mine tailings (D-MT) sample. Size fractions in which concentrations are maximized (unimodal, bimodal) or minimized (reverse unimodal) are indicated in parentheses.

Direct	Inverse		Unimodal	Bimodal	Reverse unimodal	Constant	Poor	Below detection
	Ag	Mo	Na(S3)	Ba(S4,10)	Al(S7)	S	Cr	Re
	As	Nb	Y(S8)	K(S4,10)	Ca(S4)	Se	Zr	Te
	Be	Ni	W(S8)	Mg(S1,9)	P(S5)			Hf
	Bi	Pb			Sr(S7)			Re
	Cd	Rb			Ti(S5)			
	Ce	Sb						
	Co	Sn						
	Cs	Ta						
	Cu	Te						
	Fe	Th						
	Ga	Tl						
	Ge	U						
	Hg	V						
	In	Y						
	La	Zn						
	Li	Zr						
	Mn							

Table 5
Enrichment of selected elements in the S6–S11 (⩽250 μm) size fractions of a given sample above the sample's bulk average concentrations.

Element	SM-BG (%)	SM-MT (%)	D-BG (%)	D-MT (%)	Avg. (element) (%)
As	132	62	97	69	90
Cr	111	34	26	30	50
Cu	42	152	242	206	160
Fe	50	27	48	42	42
Pb	79	90	69	70	77
Zn	60	79	78	89	76
Avg. (sample)	79	74	93	84	

Table 6
Enrichment of selected elements in the finest grained size fraction (which typically is the most highly-concentrated size fraction) above the sample's bulk average concentrations.

Element	SM-BG (%)	SM-MT (%)	D-BG (%)	D-MT (%)	Avg. (element) (%)
As	230	145	124	204	176
Cr	210	55	31	63	90
Cu	171	663	543	389	442
Fe	92	55	60	71	69
Pb	203	208	140	128	170
Zn	122	180	114	170	146
Avg. (sample)	171	218	169	159	

In cases where the concentration trend is both very pronounced and distinctive from the sample mass distribution plot, the tendency of the elemental mass distribution to follow the bulk mass distribution can be noticeably altered. Copper provides a good example of this phenomenon. The Cu concentration ranges for the D-MT and SM-BG both vary by over an order of magnitude and feature inverse trends with particle size (Fig. 5), so when combined with their respective bulk mass distributions (Fig. 3) to form elemental mass distribution plots (Fig. 6) the influence of the concentration trend results in substantial (>10%) mass distributions of Cu in the S8 (45–53 μm) and S9 (32–45 μm) size fractions. Such detailed information on the size fraction(s) in which certain toxic elements are most highly concentrated can be useful in hazardous mine waste management including mobility prediction, exposure potential, regulatory guidelines, and remediation strategies. For example, the process of wetting mine waste piles prior to excavation and relocation of the waste materials (done to minimize airborne particle mobilization) may be reconsidered if significant fractions of fine-grained particles containing elevated levels of potentially toxic elements may be mobilized through wetting and surface water runoff.

3.6. Statistical correlations

Correlation matrices for the four samples, displaying scatterplot data for each pair of elemental correlations from among the six selected elements, are shown in Fig. 7a–d. For all samples, strongly positive correlations between the selected elements are dominant, consistent with the similarities observed in particle size-dependent concentration trends (see Fig. 5 and Table 4).

An overview of the four correlation matrices reveals that As consistently accounts for the strongest correlation in each matrix; in the D-BG sample (Fig. 7a) As is most closely associated with Fe ($r = 0.981$), while the other samples feature very strong correlations between As/Pb (D-MT, $r = 0.998$), As/Cr (SM-BG, $r = 0.997$) and As/Zn (SM-MT, $r = 0.996$). Furthermore, when averaging pair correlations of the four samples, As displays one of the strongest degrees of correlation over the other selected elements. This is likely due to the exceedingly elevated concentrations of As in phases also containing these elements. For example, the naturally high abundance of Fe in all samples (ranging from 1% to 4.5%) and its strong correlations with As suggest that As may be present as a sorbed species onto Fe-(hydr)oxide surfaces or as ferric

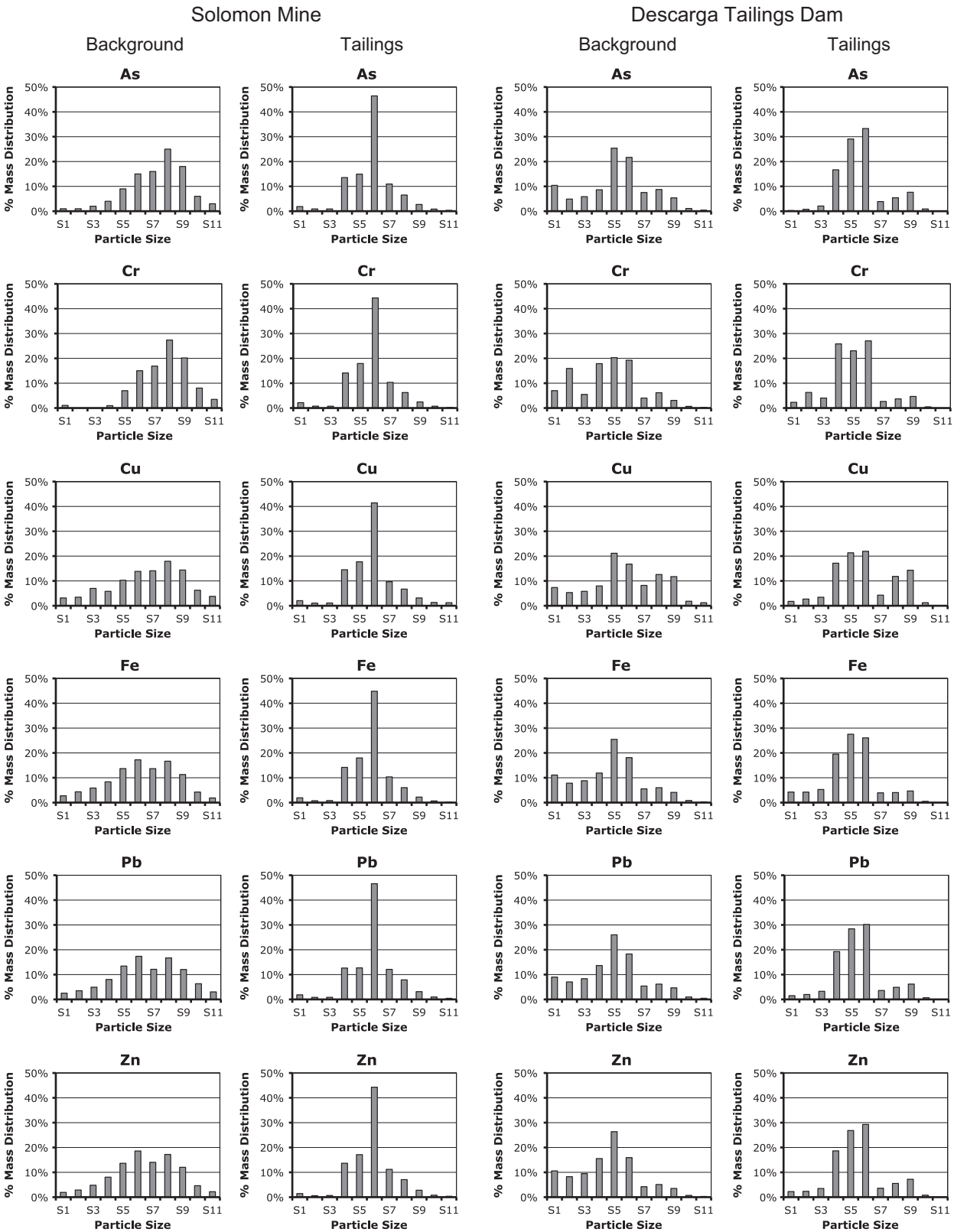

Fig. 6. Elemental mass distributions of selected elements in the Solomon and Descarga background and mine tailings samples as a function of particle size. Refer to Table 1 for a description of the particle size ranges corresponding to each labeled size fraction S1–S11.

arsenate mineral phases such as scorodite ($FeAsO_4$), arsenioside-rite, and yukonite, the latter two of which can form as secondary minerals through the oxidation of scorodite or arsenopyrite (FeAsS). Recent research from our group using synchrotron-based X-ray methods to determine the chemical speciation of As has verified the presence of such discrete As/Fe-bearing mineral phases in addition to As(V) sorbed to ferrihydrite (Kim et al., submitted for publication).

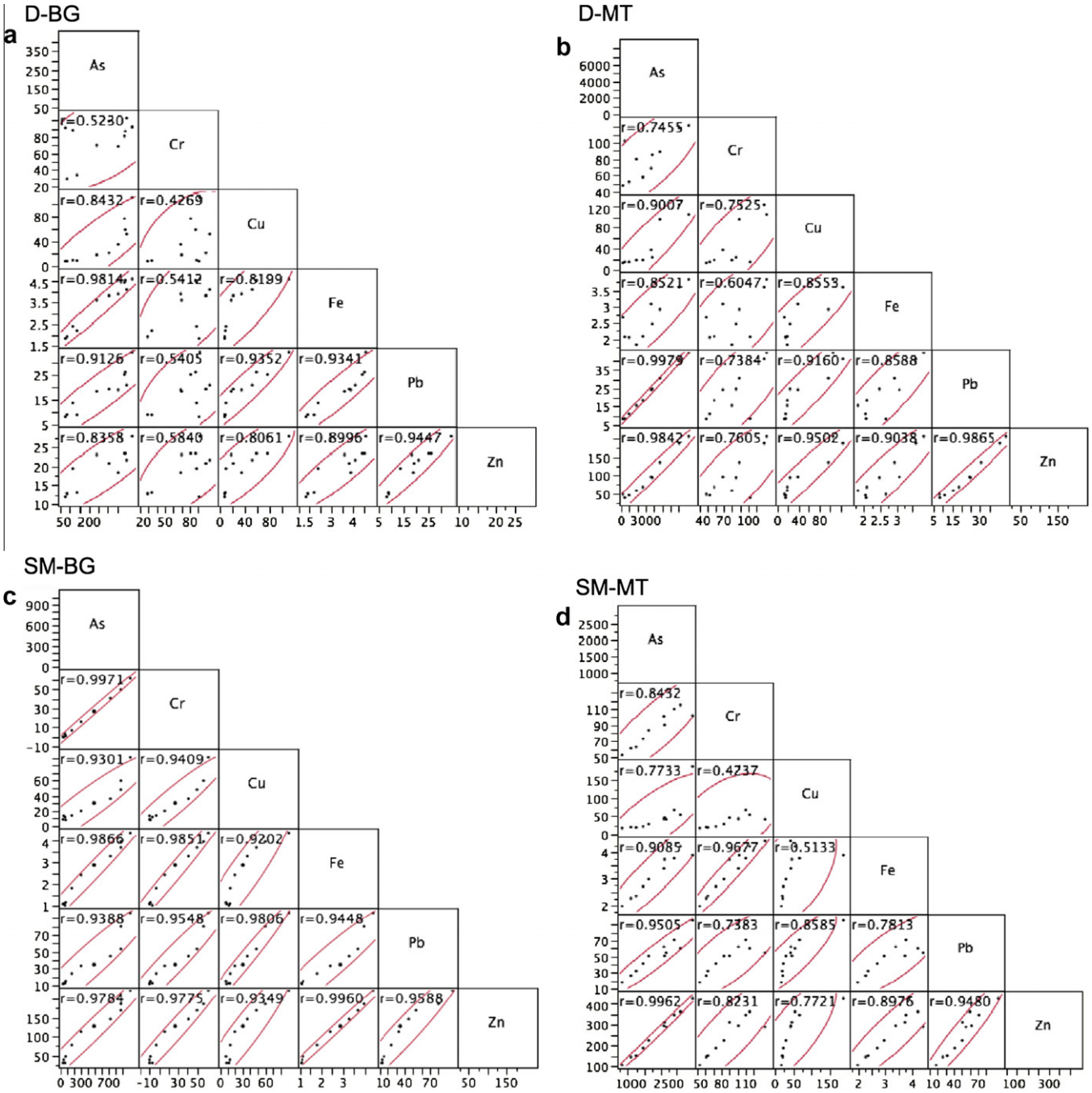

Fig. 7. Elemental correlation matrices of the (a) Descarga background (D-BG), (b) Descarga mine tailings (D-MT), (c) Solomon Mine background (SM-BG), and (d) Solomon Mine tailings (SM-MT) samples, showing the degrees of correlation between pairings of the elements selected for analysis (As, Cr, Cu, Fe, Pb and Zn). Each cell displays a 95% bivariate normal density ellipse around the points and the linear correlation coefficient for each cell's dataset. Axes are expressed in units of mg/kg (ppm) except Fe (%).

4. Conclusions

The macroscopic analytical methods described here represent a novel approach by which to characterize trends in the concentration and distribution of potentially toxic metal(loid)s as well as to identify the effects of particle size on the dispersal of and exposure to contaminated mine wastes in the environment. Notably, the results of this characterization strategy imply that regulatory policy decisions made without considering particle size effects may not be sufficient to protect biota and human health. Since state and federal screening levels for toxic metals are typically compared against bulk sample concentrations, they inherently assume that the exposure pathway is to the bulk sample and not, more accurately, to specific size fractions or particles below a certain size threshold. The finding of largely inverse trends between particle size and trace metal(loid) concentration combined with the observation that concentrations of these elements in potentially ingestible/respirable particles can exceed bulk sample average concentrations by as much as 660% suggests that exposure levels may often be several times greater than those predicted by existing methodologies. The inclusion of this documented particle size dependency on trace metal(loid) concentration should be used

to guide the understanding and development of policies that can more accurately predict the potential exposure of trace metal(loid)s to humans and other living organisms.

Acknowledgements

This work was funded by a grant from the US Geological Survey Mineral Resources External Research Program (USGS-MRERP Award # 06HQGR0181), NSF-CAREER Grant #0847811, and a subcontract from the Bureau of Land Management. Field support from BLM collaborators Dick Forester, Peter Graves, and David Lawler enabled the collection of samples from the Randsburg historic mining district. The authors wish to thank Chapman Environmental Geochemistry Laboratory undergraduate research students James Akau, Ben Deeb, Stefanie Miller, Long Nguyen, David Stack, and Eric Sugihara for their assistance with aspects of this project. Finally, reviews from Dr. Bob Seal, Dr. George Breit, and two anonymous reviewers improved this manuscript and their contributions are greatly appreciated.

Appendix A. Supplementary material

Supplementary data associated with this article can be found, in the online version, at doi:10.1016/j.apgeochem.2011.01.007.

References

Audry, S., Blanc, G., Schafer, J., 2006. Solid state partitioning of trace metals in suspended particulate matter from a river system affected by smelting-waste drainage. Sci. Total Environ. 363, 216–236.

Blanchard, M., Alfredsson, M., Brodholt, J., Wright, K., Catlow, C.R.A., 2007. Arsenic incorporation into FeS_2 pyrite and its influence on dissolution: a DFT study. Geochim. Cosmochim. Acta 71, 624–630.

Carpi, A., 1997. Mercury from combustion sources: a review of the chemical species emitted and their transport in the atmosphere. Water Air Soil Pollut. 98, 241–254.

Carrizales, L., Razo, I., Tellez-Hernandez, J.I., Torres-Nerio, R., Torres, A., Batres, L.E., Cubillas, A.C., Diaz-Barriga, F., 2006. Exposure to arsenic and lead of children living near a copper-smelter in San Luis Potosi, Mexico: importance of soil contamination for exposure of children. Environ. Res. 101, 1–10.

Chou, C., De Rosa, C.T., 2003. Case studies – arsenic. Int. J. Hygiene Environ. Health 206, 381–386.

Eggleton, R.A., 1987. Noncrystalline Fe–Si–Al oxyhydroxides. Clays Clay Miner. 35, 29–37.

EPA, 1997a. Exposure Factors Handbook. National Center for Environmental Assessment, Office of Research and Development.

EPA, 1997b. Mercury Study Report to Congress. US Environmental Protection Agency, Office of Air Quality Planning and Standards and Office of Research and Development.

Evans, M., Hastings, N., Peacock, B., 2000. Statistical Distributions. John Wiley & Sons, Inc., New York.

Hammersley, A., 2004. <http://www.esrf.eu/computing/scientific/FIT2D/>.

Harsh, J.B., Doner, H.E., 1981. Characterization of mercury in a riverwash soil. J. Environ. Qual. 10, 333–337.

Hulin, C.D., 1925. Geology and Ore Deposits of the Randsburg Quadrangle. California State Mining Bureau, California.

Jackson, T.A., 1997. Long-range atmospheric transport of mercury to ecosystems, and the importance of anthropogenic emissions – a critical review and evaluation of the published evidence. Environ. Rev. 5, 99–120.

JMP, 2007. JMP: Statistical Discovery. JMP 7.0.1. SAS Institute Inc.

Kim, C.S., Miller, S.R., Sugihara, E.S., Akau, J.A., Webb, S.M., Rytuba, J.J., submitted for publication. (Micro)spectroscopic analyses of particle size dependence on arsenic distribution and speciation in mine wastes. Environ. Sci. Technol.

Kim, C.S., Rytuba, J.J., Brown Jr., G.E., 2004. Geological and anthropogenic factors influencing mercury speciation in mine wastes: an EXAFS spectroscopic study. Appl. Geochem. 19, 379–393.

Kooner, Z.S., 1992. Adsorption of copper onto goethite in aqueous systems. Environ. Geol. Water Sci. 20, 205–212.

Lowry, G.V., Shaw, S., Kim, C.S., Rytuba, J.J., Brown, G.E.J., 2004. Macroscopic and microscopic observations of particle-facilitated mercury transport from New Idria and Sulphur Bank mercury mine tailings. Environ. Sci. Technol. 38, 5101–5111.

Manceau, A., Schlegel, M.L., Musso, M., Sole, V.A., Gauthier, C., Petit, P.E., Trolard, F., 2000. Crystal chemistry of trace elements in natural and synthetic goethite. Geochim. Cosmochim. Acta 64, 3643–3661.

Mandal, B.K., Suzuki, K.T., 2002. Arsenic round the world: a review. Talanta 58, 201–235.

Moore, J.N., Brook, E.J., Johns, C., 1989. Grain-size partitioning of metals in contaminated, coarse-grained river floodplain sediment: Clark Fork River, Montana, United States. Environ. Geol. Water Sci. 14, 107–115.

Moreno, T., Oldroyd, A., McDonald, I., Gibbons, W., 2007. Preferential fractionation of trace metals–metalloids into PM10 resuspended from contaminated gold mine tailings at Rodalquilar, Spain. Water Air Soil Pollut. 179, 93–105.

Mullins, M.J.P., Norman, J.B., 1994. Solubility of metals in windblown dust from mine waste dump sites. Appl. Occup. Environ. Hyg. 9, 218–223.

Nachtegaal, M., Sparks, D.L., 2004. Effect of iron oxide coatings on zinc sorption mechanisms at the clay-mineral/water interface. J. Colloid Interface Sci. 276, 13–23.

Peacock, C.L., Sherman, D.M., 2004. Copper(II) sorption onto goethite, hematite and lepidocrocite: a surface complexation model based on ab initio molecular geometries and EXAFS spectroscopy. Geochim. Cosmochim. Acta 68, 2623–2637.

Penn, R.L., Zhu, C., Xu, H., Veblen, D.R., 2001. Iron oxide coatings on sand grains from the Atlantic coastal plain: high-resolution transmission electron microscopy characterization. Geology 29, 843–846.

Plumlee, G.S., Ziegler, T.L., 2003. The medical geochemistry of dusts, soils, and other earth materials. In: Sherwood Lollar, B. (Ed.), Environmental Geochemistry. Holland, H.D, Turekian, K.K. (Exec. Eds.), Treatise on Geochemistry, vol 9. Elsevier, pp. 263–310.

Plumlee, G.S., Morman, S.A., Ziegler, T.L., 2006. The toxicological geochemistry of earth materials: an overview of processes and the interdisciplinary methods used to understand them. Rev. Miner. Geochem. 64, 5–57.

Roberts, D.R., Ford, R.G., Sparks, D.L., 2003. Kinetics and mechanisms of Zn complexation on metal oxides using EXAFS spectroscopy. J. Colloid Interface Sci. 263, 364–376.

Rytuba, J.J., Foster, A.L., Kim, C.S., Slowey, A.J., Lawler, D., Forester, R., 2007. Arsenic Contamination from the Kelly Silver and Yellow Aster Gold Mine Tailings, CA: A Potential Health Concern in the North-Central Mojave Desert. Geol.Soc. Am. Ann. Meeting, Abstract, 8–4.

Savage, K.S., Tingle, T.N., PA, O.D., Waychunas, G.A., Bird, D.K., 2000. Arsenic speciation in pyrite and secondary weathering phases, Mother Lode Gold District, Tuolumne County, California. Appl. Geochem. 15, 1219–1244.

Scheinost, A.C., Kretzschmar, R.S., Pfister, S., Roberts, D.R., 2002. Combining selective sequential extractions, X-ray absorption spectroscopy, and principal component analysis for quantitative zinc speciation in soil. Environ. Sci. Technol. 36, 5021–5028.

Towle, S.N., Bargar, J.R., Brown Jr., G.E., Parks, G.A., 1997. Surface precipitation of Co(II)(aq) on Al_2O_3. J. Colloid Interface Sci. 187, 62–82.

Wang, S., Mulligan, C.N., 2006. Occurrence of arsenic contamination in Canada: sources, behavior and distribution. Sci. Total Environ. 366, 701–721.

Westerlund, C., Viklander, M., 2006. Particles and associated metals in road runoff during snowmelt and rainfall. Sci. Total Environ. 362, 143–156.